RESEARCH ARTICLE

Flow dynamics and heat transfer characterization of confined multiple jets impinging on a complex surface

F. V. Barbosa[1] · S. F. C. F. Teixeira[2] · J. C. F. Teixeira[1]

Abstract

Submerged and confined multiple jet impingement is widely implemented in cooling applications since it provides high heat transfer coefficients and uniformity over the target plate. Its performance depends on several variables that make it complex and difficult to control. To understand the physical phenomena and characterize the flow field, an in-depth study, using Particle Image Velocimetry (PIV) technique and an heat flux sensor, is conducted in this study. The PIV provides relevant data, but the accuracy of the measurements depends on an effective experimental setup and a careful selection of the most appropriate tracer particles. Therefore, this work presents the purpose-built experimental apparatus and comprises an analysis of the efficiency of different seeding particles. The results demonstrate that olive oil particles are appropriate to track turbulent flows since particles with about 1 μm diameter are obtained by the seeding generator. PIV measurements highlight the complexity of the jet flow impinging on a step surface, which induces a strong flow reversal that affects the jet flow development and the interaction with the adjacent jets. The large-scale structures induced in the vicinity of the target plate are captured by the PIV, as well as the strong fountain flows generated between the adjacent jets. Compared with the flat geometry, the turbulence intensity at the central jet is around 25% higher for the 1 D step, while for the 2 D step, this increase reaches 7.5%. The increased turbulence intensity leads to an heat transfer enhancement. For the 2 D step plate, the Nusselt number recorded is 25% greater than the flat plate. Through this study, relevant insights for several engineering applications that use multiple jet impingement are provided, highlighting that the combination of PIV and heat flux sensors are appropriate to characterize the jet's flow dynamics and the heat transfer of this complex process.

List of symbols

D	Diameter (m)
g	Gravitational acceleration (m/s^2)
Gr	Grashof number (–)
h	Heat transfer coefficient (W/m^2 K)
H	Nozzle-to-plate distance (m)
k	Thermal conductivity (W/mK)
$\overline{\mathrm{Nu}}$	Average Nusselt number (–)
$\overline{q}$	Average heat flux (W/m^2)
Q	Dimensionless second invariant of the velocity gradient tensor (–)
Re	Reynolds number (–)
Ri	Richardson number (–)
S	Strain rate (Pa)
t	Time (s)
T	Temperature (K)
TI	Dimensionless turbulence intensity (–)
u	Uncertainty/velocity (dependent variable)/(m/s)
$\overline{U}$	Average velocity (m/s)
V	Volume (m^3)
x, y, z	Cartesian coordinates (–)
u, v, w	Velocity according to the cartesian coordinates (m/s)

Greek letters

β	Response phase (–)
β^*	Coefficient of volumetric expansion (–)
Δx	Thickness (m)
ε	Random error (dependent variable)
μ	Dynamic viscosity (Pa/s)

✉ F. V. Barbosa
flaviab@dem.uminho.pt

S. F. C. F. Teixeira
st@dps.uminho.pt

J. C. F. Teixeira
jt@dem.uminho.pt

[1] MEtRICs R&D Center, Department of Mechanical Engineering, School of Engineering, University of Minho, Guimarães, Portugal

[2] ALGORITMI R&D Center, Department of Production and Systems, School of Engineering, University of Minho, Guimarães, Portugal

η	Amplitude ratio (–)
ρ	Density (kg/m^3)
σ	Standard deviation (–)
υ	Kinematic viscosity (m^2/s)
ω	Dimensionless vorticity (–)
Ω	Angular frequency (1/s)

Subscripts

∞	Ambient air
j	Jet
max	Maximum
RMS	Root mean square
w	Wall

1 Introduction

Submerged and confined multiple jet impingement process has been implemented in several engineering applications since it allows high heat transfer rates and a uniform cooling or heating of the target surface (Ekkad and Singh 2021). However, the complexity of this flow continues to encourage researchers to provide scientifically-based solutions to the industry that reduce product defects and increase process efficiency. The multiple jet impingement is a forced convection process that involves several variables, from the jet flow parameters (velocity and temperature) to the target surface and process geometry (nozzle-to-plate distance, ribs, etc.) (Barbosa et al. 2023). The correct combination of these process variables enhances the flow interactions and increases the heat transfer performance. In this context, several experimental and numerical studies have been conducted to fully characterize the flow field and heat transfer of the multiple jet impingement process (Brakmann et al. 2016; Shariatmadar et al. 2016; Spring et al. 2012; Caliskan et al. 2014; Xing et al. 2010; Yong et al. 2015; Weigand and Spring 2011). The flow complexity is increased if submerged and confined multiple jets are implemented. This configuration is mainly used for the cooling or heating of surfaces in reflow soldering and drying processes. However, the detailed characterization of this convective process is challenging due to the strong interactions between jets combined with the complexity of the target surface. Some relevant studies in this domain are discussed below.

Geers et al. (2004) studied the velocity field and turbulence fluctuations in a hexagonal array of circular jets and observed that the central jet has the highest turbulent kinetic energy, highlighting the strong interaction with the adjacent jets. Goodro et al. (2007) analyzed the effect of Mach number and Reynolds numbers on an array of jets and concluded that the jet impingement presents a strong dependence on Mach number when greater than 0.2. Xing et al. (2010) characterized numerically and experimentally, through

TLC (Thermochromic Liquid Crystals), the heat transfer of inline and staggered arrays and concluded that, independently of the crossflow, the inline pattern outperforms the staggered one. Ichikawa et al. (2016) studied the flow of multiple circular impinging jets through PIV and found that small impinging distances (*H/D*) and jet-to-jet spacings (*S/D*) increase the jet's momentum around the impingement, inducing a larger and stronger roll-up vortex structure. Terzis (2016) analyzed the flow field and surface heat transfer using PIV and Liquid Crystal Thermography (LCT) and observed that the increase in thermal transport and near-wall mixing promotes heat transfer. Li et al. (2018) studied the flow and heat transfer of parallel multiple jets impinging on a flat surface using numerical transient simulations and experimental oil flow visualization and found that grooves induced over the target plate are mainly triggered by the jet's interaction. They also combine TLC technique to study the heat transfer distribution of multiple jets impinging on a half-smooth and half-rough target plate. Their results show an enhancement of more than 50% using half-rough surfaces. Tepe et al. (2020) experimentally investigated the effect of the rib-roughened surface on jet impingement cooling using a TLC technique. The authors found that the highest average Nusselt number is obtained for *H/D* = 3 at Re = 32,500 while for Re ≤ 27,100 the optimized heat transfer coefficient is obtained for *H/D* = 2. In their turn, Ren et al. (2021) experimentally investigated the influence of micro-cooling units on jet impingement, inducing an increase of 20–300% as the height of these microstructures increase. Lo and Liu (2018) applied transient target plate and found that the pressure loss is not increased by microstructures on the plate but the heat transfer is improved. Barbosa et al. (2022) analyzed the jet's flow structure by PIV and observed that thicker wall jets are induced for lower *H/D* due to stronger interactions between jets and the surrounding air in a confined space. It seems that by increasing *H/D*, larger primary vortices with a weaker magnitude are generated.

The literature review shows that although several studies have been conducted in the multiple jet impingement field, looking at the influence of different process variables on heat transfer performance, fewer studies characterize the flow structures over complex surfaces and make the correspondence with convective heat transfer. In this context, the present study contributes to the scientific field by focusing on the analysis of the flow dynamics of multiple air jets impinging on a plate with a step, using a 2-D PIV system combined with a heat flux sensor. The results are compared with a flat plate to highlight the relevance of the plate geometry in both heat transfer and jet flow structure. The measurements provide relevant insights regarding the velocity, vorticity, and turbulence intensity profiles. Moreover, the 2nd invariant field is analyzed, providing important information regarding the flow structure induced between the jet orifice and

the target plate. The average Nusselt number over the target surfaces is obtained from heat flux data and the plate geometry that ensures higher heat transfer rates are identified. This study provides relevant data that can contribute to solve industrial problems, as is the case of the reflow soldering process. Reflow soldering is one stage of the Surface Mount Technology (SMT) used to produce Printed Circuit Boards (PCBs) integrated into all electronic devices that make part of our daily lives (Whalley 2004). Considering the complexity of the PCBs and the complicated thermal response as the PCBs are heated and cooled inside the reflow oven, soldering failures such as cold and/or hot spots, insufficient wetting and overheating joints occur, leading to a productivity loss corresponding to roughly 30–50% of the total manufacturing costs (Costa 2015; Tsai 2012). To enhance the process and minimize product defects, it is crucial to characterize both flow dynamics and heat transfer in the vicinity of the step structure. Therefore, this work is conducted using a Reynolds number equal to 5000, which corresponds to that implemented in the industrial process, providing specific insights for a real-case scenario.

2 Experimental methods

In this section, the experimental setup, specially designed and constructed to conduct the heat transfer and PIV measurements, is presented. Besides the experimental setup, relevant details of the PIV technique are described, focusing on the selection of the appropriate seeding particles to conduct accurate measurements.

2.1 Experimental setup

The experimental setup was specially built to conduct PIV and heat transfer measurements of submerged and confined multiple air jets impinging on a target plate. The test rig, presented in Fig. 1a, is composed of a setup structure, the 2-D PIV system (laser, CCD camera, and computer for data processing), the seeding generator, and the heat flux sensor. Figure 1b and c shows with higher detail the measuring zone. The laser sheet crosses the central jet as well as two adjacent jets located on both sides. However, even if the effect of the jets located at the front and back rows are not directly captured by the camera, these jets influence the overall jet flow development since a staggered configuration is implemented. As shown in Fig. 1d and e, the heat flux sensor is mounted over the target plate to provide data regarding heat transfer. The position of the jets regarding the heat flux sensor is schematically presented in Fig. 1f, showing that a total of 7 jets impinge the sensor. Therefore, the average heat transfer presented in this work refers to these same jets.

The experimental setup consists of a centrifugal fan that blows downward ambient air into an acrylic plenum to stabilize the flow and reduce turbulence. The seeding particles are introduced inside this box, to ensure a uniform mixing with ambient air. A honeycomb structure is placed at the top of the tube to promote the uniformization of the flow. At the bottom of this tube, a nozzle plate with an array of circular orifices is placed to generate the air jets. The seeded air flows through the circular nozzles with 5 mm in diameter, spaced by $S/D = 3$, and impinges a target plate spaced $H/D = 2$. These parameters are selected based on a Design of Experiments (DoE), using Taguchi's method, conducted
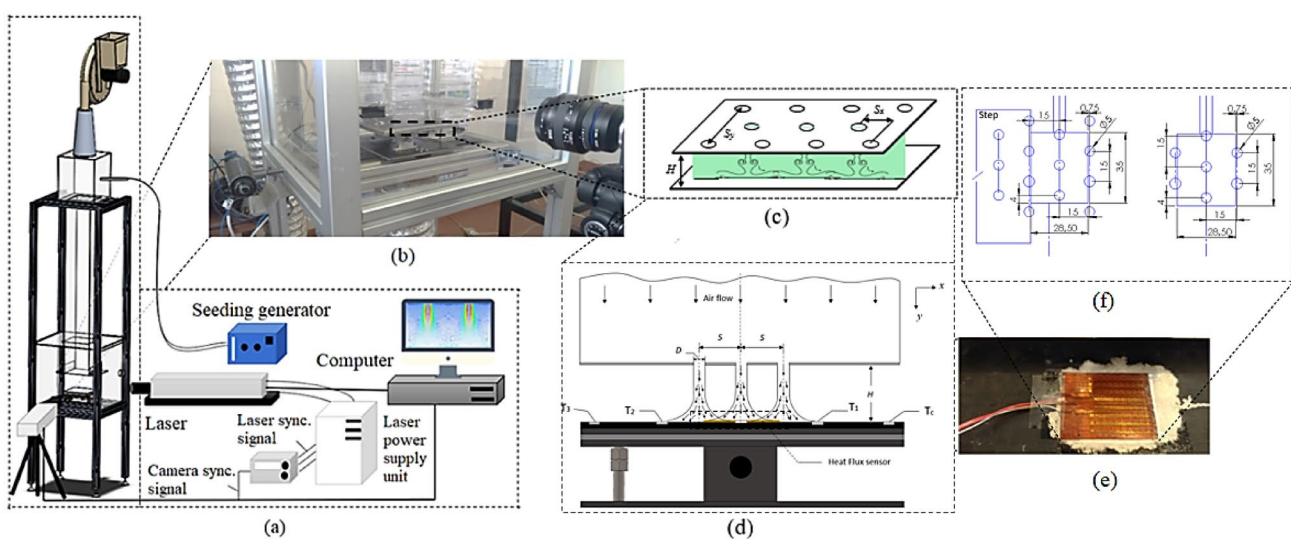
Fig. 1 Experimental setup: **a** test rig; **b** measurement zone; **c** impinging region; **d** target plate; **e** heat flux sensor; **f** location of the jets impinging over the heat flux sensor

by Barbosa et al. (2021), which shows that the combination between these variables lead to an higher heat transfer rate. The measuring area is surrounded by an acrylic box that minimize the interference of the environment. The transparency of this box is crucial to ensure the correct operation of the PIV since a clear passage of the laser beam provides a correct illumination of the measuring region. Moreover, the refraction of light is another important parameter, being important to ensure that the test section walls and the seeding particles have closely matched refractive indices to minimize measurement errors. According to Merzkirch (1987), and considering that the laser emits light at a wavelength of 532 nm, the refractive index (n) of the acrylic material is approximately 1.49, while n of seeding particles is addressed in Sect. 3.

To ensure a uniform heating of the target plate, a 1000 W, 200×200 mm mica heater is placed between two support plates. The control of the target plate temperature is ensured by a thermocouple connected to a *Selec* TC544 temperature controller. To measure the convective heat transfer, an OMEGA® HFS-4 thin film heat flux sensor, rated at a maximum of 94,500 W/m², is mounted at the center of the target surface, as it can be observed in Fig. 2. Two target plate configurations are studied, a flat plate, Fig. 2a and a non-flat plate Fig. 2b. The second case involves two different step heights corresponding to y/D equal one a two.

2.2 Heat transfer measurements

The OMEGA® HFS-4 thin-film heat flux sensor provides data regarding the mean heat flux, according to Eq. (1).

$$\overline{q} = -k_{t-f}\left(\frac{\Delta T}{\Delta \delta}\right) \tag{1}$$

The mean heat flux, $\overline{q}$, is given by the temperature difference, ΔT, measured across the electrically insulating layer, Kapton®, with a thickness of $\Delta \delta = 0.18$ mm and a thermal conductivity, k_{t-f}, of 0.045 W/m·K (Assaad et al. 2008). The information provided by the manufacturer shows that the output given by the heat flux sensor at 21.1 °C is equal to 2 μV/(W/m²). Considering a correction factor that varies with the operation temperature, a value of 1.8 μV/(W/m²) is considered since the sensor will operate at temperatures close to 120 °C. Taking this information into account, the Seebeck coefficient is equal to 4.01 μV/°C.

2.3 PIV measurements

The PIV technique has been widely used to measure the velocity field of flow, providing detailed information about the impinging jet's flow dynamics (Geers et al. 2004; Ichikawa et al. 2016; Angioletti et al. 2003; Khayrullina et al. 2017; Nebuchinov et al. 2017; Gnanamanickam et al. 2019; Singh and Prasad 2020). Using this method, it is intended to characterize, at a macro-scale, the flow behavior over the target surface, but also to identify, at a micro-scale, the phenomena that occur in the vicinity of surface transition (such as back steps and forward steps). The 2D-PIV system applied in this study (Fig. 3) consists of a 145 mJ double-pulse Nd:YAG laser that induces a light sheet firing on the second harmonic, i.e., green (532 nm). A two-dimensional laser sheet is obtained by the two beams previously recombined on the same optical path by a polarized dichroic filter and expanded in one direction through a combination of spherical and cylindrical lenses (Angioletti et al. 2003). The laser sheet illuminates the measurement region, from the exit of the nozzles to the target plate over the length of the test chamber. The light scattered by the seeding particles is captured by the HiSense Zyla CCD camera, positioned perpendicularly to the laser sheet. The CCD camera is equipped with a 50 mm Zeiss lens with a pixel resolution of 2560×2160 (5.5 Megapixels).

To conduct the measurements, three inputs are introduced: the time between two laser pulses, i.e., the time difference between the two-particle images, $\Delta t = 50$ μs; the trigger rate, i.e., the sampling frequency of the PIV setup ($f = 15$ Hz); and the number of images required for acquisition (100 images by acquisition). Δt was defined by previous measurements that allow to determine the best compromise between Δt accuracy and the flow velocity. The measurements are performed using a double frame mode through which the camera acquires one single frame for each trigger pulse. Considering that the time between each pulse defines the exposure time, the camera is triggered twice in double frame mode giving the double exposure enough to be able to capture on time the required number of particles per interrogation area. The data acquisition and image processing are performed using the software Dynamic Studio.

Fig. 2 Target plate configurations: **a** flat plate; **b** non-flat plate. Figures show the location of the heat flux and each number correspond to the location of thermocouples
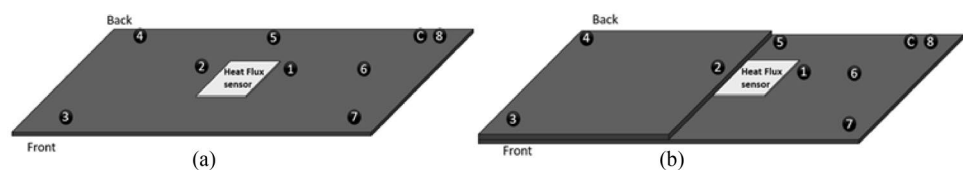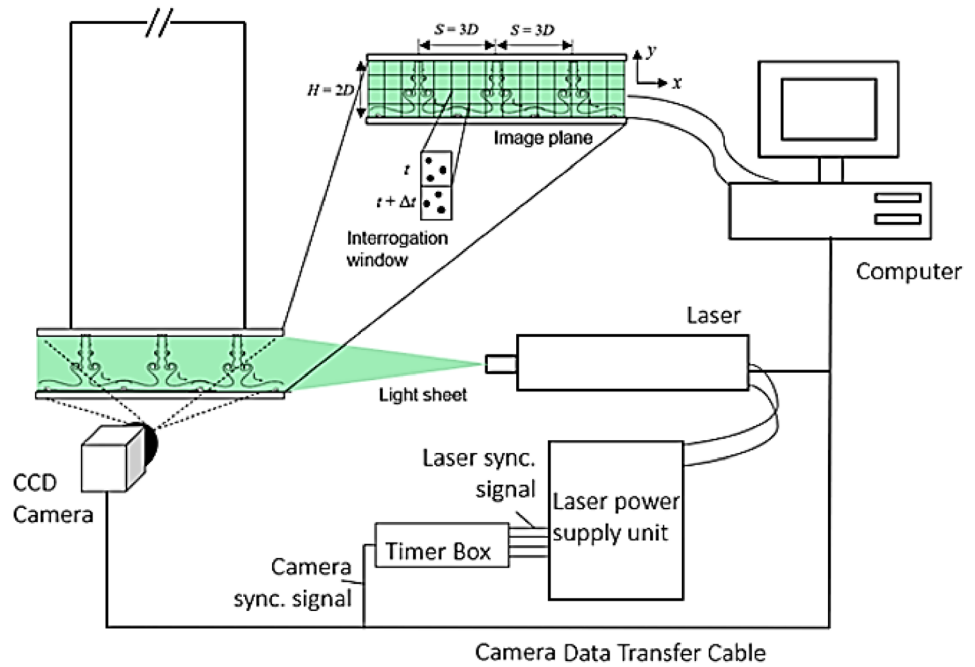
Fig. 3 2-D PIV system

2.4 Seeding particle's size measurements

Seeding particles play an important role in the accuracy of the PIV measurement. According to Melling (1997), the tracer particles should not affect the dynamics of the flow neither changing their properties during the measurement nor interacting with each other. Furthermore, they must be randomly and uniformly distributed across the flow with an appropriate concentration to increase the accuracy of the measurements. However, achieving an optimum seeding flow is the most difficult task of the PIV experiments. To ensure the precise distribution of the seeding throughout the measurement region, the selection of the proper seeding particle's size and material is crucial. According to Grant (1997), a compromise between a small particle size of low inertia, to improve the flow tracking, and a large particle size to improve the light scattering, easily detected by the camera, must be ensured. Moreover, a compromise between the dimension of the seeding particles and their concentration is required to obtain accurate velocity fields. Due to the importance of the selection of tracer particles for the tracking of the flow, a seeding characterization is conducted in this work and the results are presented in Sect. 3.

To measure the particle's diameter a Laser Diffraction Technique is applied using a Malvern 2600 HSD. This method, depicted in Fig. 4, uses a low-power He–Ne laser that forms a collimated beam of light. If the beam strikes a particle, light is scattered and it is subsequently collected by a receiver lens which operates as a Fourier transform lens forming the far-field diffraction pattern of the scattered light at its focal plane. This scattered light is subsequently

gathered over a range of solid angles of scattering, by a detector that consists of 31 concentric annular sectors. The unscattered light passes through a small aperture in the detector and out of the optical system, being monitored to determine the volume concentration of the sample. The diffraction angle increases with decreasing particle size and the number of particles can be obtained through the intensity of the diffracted beam at any angle (Eshel et al. 2004). To obtain an accurate measurement, it is recommended that the number of particles in an experiment varies between 100 and 10,000.

To analyze the results obtained by the Malvern 2600 HSD, the Model Independent Analysis is selected (Kowalczuk and Drzymala 2016). This mode estimates a volume distribution based on the measured light energy, assuming a 15 degree polynomial and new light energy distribution is calculated using Eq. (2) while the residual difference is calculated by Eq. (3):

$$D_j = U_{i,j} V_i \tag{2}$$

$$\mathrm{Log} D = \mathrm{Log}_{10}\left(\sum (D_j - L_j)^2 \right) \tag{3}$$

where i is the index of the size band, j is the index of detector elements, $U_{i,j}$ describes how particles in size band i scatter light to detector element j. D_j is the measured data, V_i the relative volume of material contained in the particles in size band i and L_j the data was calculated from the estimated volume distribution. A new set of values of L_j is calculated

Fig. 4 Experimental setup scheme for the measurement of the particle's diameter
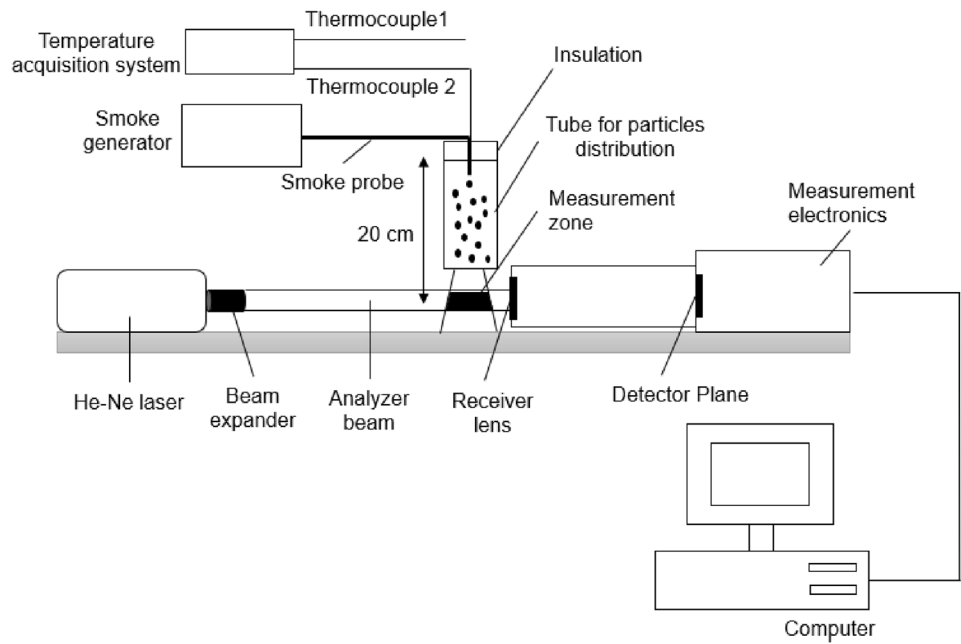
from the difference between D_j and L_j. This is an iterative process that stops when the residual reaches a minimum.

The measurement yields a volume distribution of the dispersed material throughout the 32 bands. Since the main interest of the measurement is to obtain a particle diameter, the volume distribution must be converted into a diameter. The derived diameter usually used in this type of measurement is the Sauter Mean Diameter (SMD), $D_{3,2}$, since the ratio of volume to surface area for the Sauter mean is the same as the ratio for the entire volume of particles (Kowalczuk and Drzymala 2016). This parameter is calculated through Eq. (4), where d_i represents the mean diameter of size band i, n_i is the number fraction in band i.

$$D_{3,2} = \frac{\sum n_i d_i^3}{\sum n_i d_i^2}. \tag{4}$$

2.5 Data reduction and uncertainty analysis

To determine the heat transfer induced by submerged and confined multiple jets impinging on flat and non-flat plates, the average Nusselt number ($\overline{\mathrm{Nu}}$) is calculated. In this study, $\overline{\mathrm{Nu}}$ is obtained by using the data provided by the heat flux sensor. As expressed in Eq. (5), $\overline{\mathrm{Nu}}$ depends on the average convective heat transfer coefficient ($\overline{h}$), the mean nozzle diameter ($\overline{D}$), and the thermal conductivity of the fluid (k). While the mean diameter of the nozzle is determined by averaging the measurement of 10 orifices diameters of the nozzle plate, k is temperature-dependent obtained directly from the literature (Cengel and Ghajar 2011).

$$\overline{\mathrm{Nu}} = \frac{\overline{h} \cdot \overline{D}}{k} \tag{5}$$

where $\overline{h}$ is given by the heat flux, $\overline{q}$, measured by the heat flux sensor, the average plate temperature ($\overline{T_w}$) and the jet's average temperature ($\overline{T_j}$), as described in Eq. (6):

$$\overline{h} = \frac{\overline{q}}{\left(\overline{T_w} - \overline{T_j}\right)} \tag{6}$$

To estimate the uncertainty of the Nusselt number, the method presented by the ASME 98 (ASME 1998) for uncertainty quantification is followed, being expressed by Eq. (7).

$$u_{\overline{\mathrm{Nu}}} = \sqrt{\left(\frac{\partial \overline{\mathrm{Nu}}}{\partial \overline{h}} u_{\overline{h}}\right)^2 + \left(\frac{\partial \overline{\mathrm{Nu}}}{\partial \overline{D}} u_{\overline{D}}\right)^2 + \left(\frac{\partial \overline{\mathrm{Nu}}}{\partial k} u_k\right)^2} \tag{7}$$

In its turn, $\overline{h}$ depends on $\overline{q}$, $\overline{T_w}$ and $\overline{T_j}$, meaning that the uncertainty of measurements of these parameters is propagated to the result and must also be considered. The heat transfer coefficient uncertainty is obtained by Eq. (8).

$$u_{\overline{h}} = \sqrt{\left(\frac{\partial \overline{h}}{\partial \overline{q}} u_{\overline{q}}\right)^2 + \left(\frac{\partial \overline{h}}{\partial \Delta \overline{T}} u_{\Delta \overline{T}}\right)^2} \tag{8}$$

In addition, while $\overline{q}$, and $\Delta \overline{T} = \overline{T_w} - \overline{T_j}$, are instantaneously recorded by the data acquisition system and analyzed following the method previously expressed; the uncertainty of $\overline{D}$ results from the statistical analysis of the measurements obtained with the caliper, leading to an average value of 4.92 mm with an uncertainty of 2.45×10^{-2} mm. Regarding k, the theoretical values are obtained from the

literature (Cengel and Ghajar 2011). Since k varies linearly with temperature ($20\,°C < T_j < 35\,°C$), k is calculated for each air jet temperature recorded by the thermocouple using Eq. (9).

$$k = 7 \times 10^{-5} T_j + 2.366 \times 10^{-2} \tag{9}$$

This shows that, since k is a variable that depends on T_j, the uncertainty of this parameter must also be propagated to the result. The thermal conductivity uncertainty is calculated through Eq. (10). Equations (7), (8), and (10) follow the theoretical concepts presented in ASME (1998).

$$u_k = \sqrt{\left(\frac{\partial k}{\partial \Delta T} u_{\Delta T}\right)^2} \tag{10}$$

$u_{\overline{q}}, u_{\Delta T}, u_{\overline{h}}, u_D, u_k$ (Eqs. 7, 8, and 10) represent the uncertainty of heat flux, temperature, heat transfer coefficient, diameter, and thermal conductivity, respectively. Since the total uncertainty of the Nusselt number is given by both random and systematic errors the procedure must be applied for each error type. This means that, $u_{\overline{q}}, u_{\Delta T}, u_{\overline{D}}$, previously presented are assumed as random uncertainties, while for the calculation of systematic uncertainties, $u_{\overline{q}}, u_{\Delta T}, u_{\overline{D}}$ assume the values presented in Table 1.

Regarding this study, uncertainty related to temperature measurements is about 0.2%, while, regarding the Nusselt number, this value is extended to 1.5%.

The velocity measured by the PIV system, U, is composed of two components, in x direction and y direction, being the uncertainty expressed by u_{Ux} and u_{Vy}, respectively. In this specific case, $u_{Ux} = u_{Vy} = u_U$, and it can be obtained by Eq. (11), which depends on the time between pulses, Δt, the scale factor variation, ΔSc, and the particle's displacement, Δx_p.

$$u_U = \sqrt{\left(\frac{\partial U}{\partial(\Delta S_c)} u_{S_c}\right)^2 + \left(\frac{\partial U}{\partial(\Delta x_p)} u_{x_p}\right)^2 + \left(\frac{\partial U}{\partial t} u_t\right)^2} \tag{11}$$

Since the time between pulses Δt, can be considered infinitely small, for a certain range of flow turbulence, its contribution to the velocity uncertainty can be neglected, simplifying the equation in Eq. (11) into Eq. (12):

$$u_U = \sqrt{\left(\frac{\partial U}{\partial(\Delta S_c)} u_{Sc}\right)^2 + \left(\frac{\partial U}{\partial(\Delta x_p)} u_{\Delta x_p}\right)^2} \tag{12}$$

Sciacchitano et al. (2013) presented a methodology for uncertainty quantification of PIV systems, known as the discrete window offset technique. This method consists of the statistical analysis of the matched particle image disparity, which is the residual distance between two consecutive particle images obtained after the matching. For more information regarding this uncertainty estimation procedure refer to Westerweel (1997). This method was used to quantify the uncertainties related to the PIV measurements. Thus, it was found that the uncertainties related to the Reynolds number are about 4%, while the mean velocity uncertainties throughout the domain are approximately 10%.

2.6 Experimental conditions

The experiments consist of air that flows through circular nozzles spaced $H = 2\,D$ from the target plate, inducing turbulent multiple jets (Re = 5000) which impinge different plate configurations: a flat plate, and two non-flat plates with 1 D and 2 D steps. The jets follow a staggered configuration and are spaced 3 D in both spanwise (S_y) and streamwise (S_x) directions. These geometrical parameters were selected tacking into consideration the study conducted by Barbosa et al. (2021) that shows that the optimized configuration for multiple air jets impinging on a surface corresponds to a staggered array, $H/D = 2$ and $S/D = 3$. The row illuminated by the laser sheet contains the central jet and two adjacent jets, one on each side. Even if the measuring zone is totally open, the effect of the outlets on the impingement only can be considered on the right and left-hand sides of the target plate, since a total of nine rows (four on each side of the central row) are used. The mean of the jets and plate temperatures are equal to 22 °C and 120 °C, respectively. The measured variables—heat flux, air jets and plate temperatures—were recorded over a time span of 30 min, and to ensure the repeatability of the experiments, a total of three tests, for each plate configuration, were carried out consecutively.

3 Results and discussion

This section presents the selection of the seeding particles based on the experimental measurement conducted with the Malvern 2600. The PIV measurements are then conducted and the results are expressed in terms of velocity, turbulence intensity, vorticity, and 2nd Invariant. Results also include

Table 1 Systematic uncertainties

Source	Measurement method	Uncertainty
Density	Tabled value (Cengel and Ghajar 2011)	$\pm 3 \times 10^{-6}$ (kg/m³)
Heat flux	Heat flux sensor	± 0.58 (W/m²)
Nozzle diameter and heat flux sensor area	Caliper	± 0.01 (mm)
Target and jets temperature	Type K thermocouples	± 0.12 (°C)

the average heat transfer over the three target plates, 2 *D* step, 1 *D* step, and flat.

3.1 Selection of the seeding particles

Three different liquid flows are selected to conduct the study, Shell Ondina EL oil, Johnson Baby oil, and olive oil. The Shell Ondina EL oil is typically used with the Concept Smoke Aerotech system, while olive oil is pointed out by several authors as a good flow seeding (Melling 1997). Due to the unpleasant smell released by the vaporized olive oil, the Johnson Baby oil is also tested in this work.

To determine the size of different seeding particles, measurements are conducted using the Malvern 2600 HSD and the Model Independent Analysis, previously presented, is used for data analysis. The measured seeding particle's diameter for each tested flow is presented in Table 2. These values were obtained for the best combination of temperature and flow rate of the Concept Smoke Aerotech seeding generator.

The data show that olive oil yields to the lower seeding particle size, while the Shell Ondina EL oil presents the higher value. To determine the ideal particle's diameter for this specific flow, whose Re = 5000, the particle's response in turbulent flows is analyzed considering the equation of motion of a suspended sphere (Basset 1888). For particle response in turbulent flows, the equation of motion can be expressed by the amplitude ratio, η, and the response phase β of the instantaneous particle and fluid motions.

According to Hinze (1975), the flow and particle velocities can be expressed using Fourier integrals, as presented in Eqs. (13) and (14), respectively.

$$U_f = \int_0^\infty \left(\alpha' \cos \Omega t + \lambda \sin \Omega t \right) d\Omega \tag{13}$$

$$U_p = \int_0^\infty \eta \left[\alpha' \cos (\Omega t + \beta) + \lambda \sin (\Omega t + \beta) \right] d\Omega \tag{14}$$

where Ω is the angular frequency of the fluid motion. The second equation shows that the response of the particle to the fluid turbulence is lagged by β, given by Eq. (15), with an amplitude corrected by a factor η (Eq. 16), that is below the unit.

Table 2 Sauter mean diameter (SMD) measured by Malvern 2600

Value ± 0.01 [μm]		
Olive oil	Johnson baby oil	Shell Ondina EL oil
0.82	4.84	14.30

$$\beta = \tan^{-1} \left(\frac{f_2(\Omega)}{1 + f_1(\Omega)} \right) \tag{15}$$

$$\eta = \left[\left[1 + f_1(\Omega) \right]^2 + f_2^2(\Omega) \right]^{1/2} \tag{16}$$

where f_1 and f_2 are expressed in detail in Hinze (1975). β and η are values that vary in function of the fluid oscillation frequencies, the fluid physical properties, and the dimension of the particles. If $\rho_p/\rho_f = 1$, the particles track the flow regardless of their size. In this study, the seeding particles used are olive oil with a density of 908.7 kg/m³, at ambient temperature (Sahasrabudhe et al. 2017), and the flow is air whose density and dynamic viscosity at ambient temperature are 1.204 kg/m³ and 1.825×10^{-5} kg/m s, respectively. To analyze the behavior of the olive oil droplets motion in air, in amplitude and phase, with the variation of the oscillation frequency, two graphs are plotted and presented in Figs. 5 and 6.

From the concepts presented above, the olive oil droplet only can be considered an ideal seeding particle for fully turbulent flows if η is close to 1. If the oscillation frequency of the flow is lower than 10,000 Hz, olive oil particles with a diameter slightly higher than 1 μm can be applied. However, if $\Omega > 10,000$ Hz, a diameter of 1 μm must be ensured. These conclusions are in agreement with (Melling 1997).

To determine the range of the flow frequency, PIV measurements are conducted and the vorticity magnitude is determined. Vorticity is defined as the curl of the velocity field, as expressed in Eq. (17).

$$\vec{\omega} = \nabla \times \vec{u} \tag{17}$$

The results show that the flow frequency for Re = 5000 is close to 13,000 Hz. Combining these results with the data presented in Table 2, it is clear that olive oil is the seeding particle that complies with the requirements. The last comment related to the seeding particles concerns the refractive index. As previously mentioned, it is important to ensure that the materials used for flow visualization, i.e., test section walls and seeding particles, have closely matched refractive indices (Merzkirch 1987). Considering that olive oil has a refractive index varying between 1.44 and 1.47 and this value for the acrylic walls is equal to 1.49, it can be concluded that the olive oil particles are a good choice to conduct the PIV measurements.

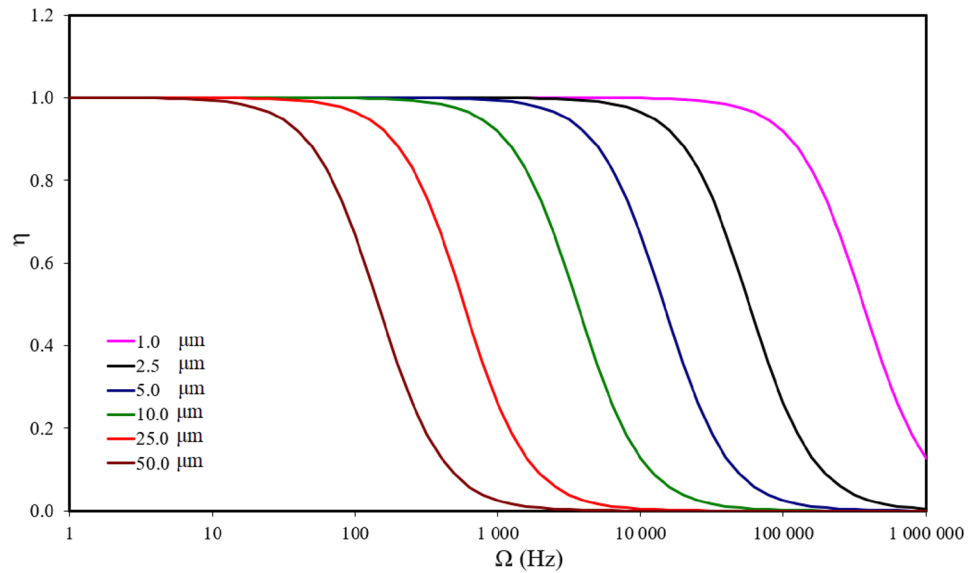## 3.2 Influence of the target plate geometry on the jet's flow dynamics

In this section, attention is provided to the influence of the target plate geometry on the jet's flow structure. Therefore,

Fig. 5 Response in amplitude of olive oil droplets in air for different particles diameter

**Fig. 6** Response in phase of olive oils in air at different particles diameter

### 3.2.1 Time-averaged velocity profiles

The effect of the target plate geometry is analyzed by comparing the velocity profiles obtained from the PIV measurements. The results are presented from Figs. 7, 8 and 9, regarding flat, 1 *D* step, and 2 *D* step plates, respectively. Starting with an overall analysis of the velocity fields, the data clearly show the effect of confinement on the generation of the different jet flow regions. The small distance between the nozzle and the target plate ($H/D = 2$) has a strong influence on the flow development at the jet axis since the flow is within the length of the potential core $H/D < 6$

the central row of three different plate configurations is analyzed, 1 *D* step, 2 *D* step, and flat plate.

(Livingood and Hrycak 1973). Therefore, maximum velocities are recorded from the inlet to the surface, and no decaying or fully developed regions are identified. As the flow gets closer to the wall, the axial component momentum is converted into an accelerated horizontal component, flowing in direction to the outlets. Along the way, the wall jets interact, inducing fountain flows at $x/D = 3$, in all figures, and at $x/D = -3$ and 3, in Fig. 7.

Focusing in Fig. 7b, the velocity profile near the target plate shows that the central jet ($x/D = 0$) presents higher velocities near the stagnation region when compared with the other adjacent jets. This behavior can be explained by the wall jet interactions and jet induced crossflow, which generate a slight deflection of the adjacent jets. The interaction between the wall jets induces a fountain flow, expressed by
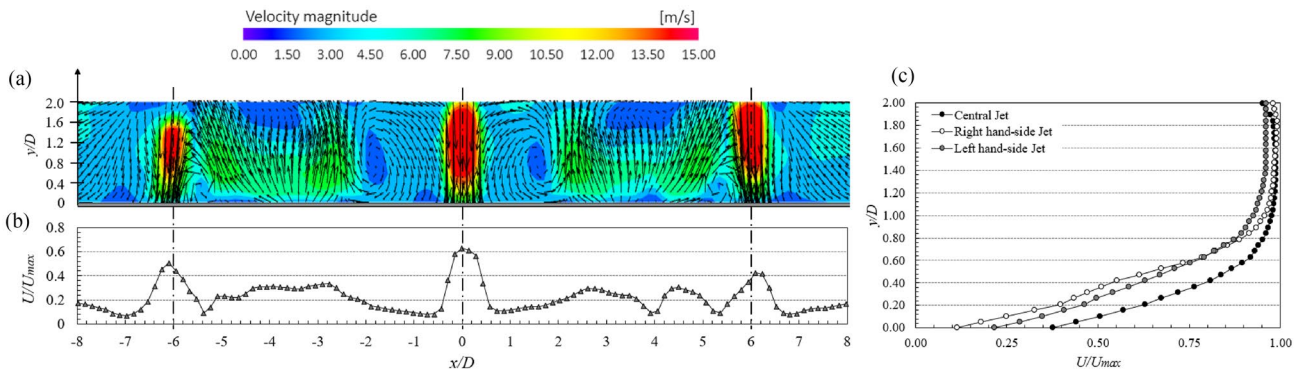
Fig. 7 Flat plate case velocity profile: **a** velocity field; **b** over the target plate at $y/D = 0.15$; **c** at the jet's axes
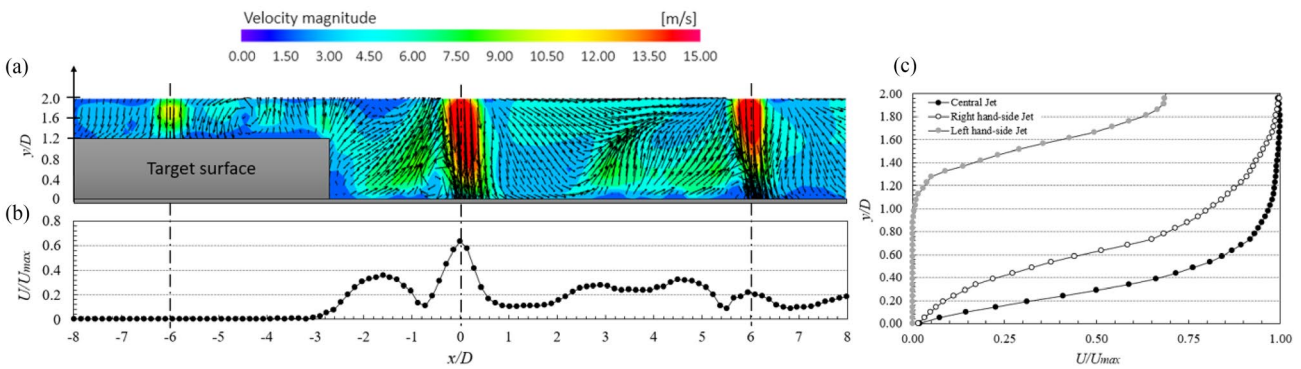
Fig. 8. 1 D step plate case velocity profile: **a** velocity field; **b** over the target plate at $y/D = 0.15$; **c** at the jet's axes
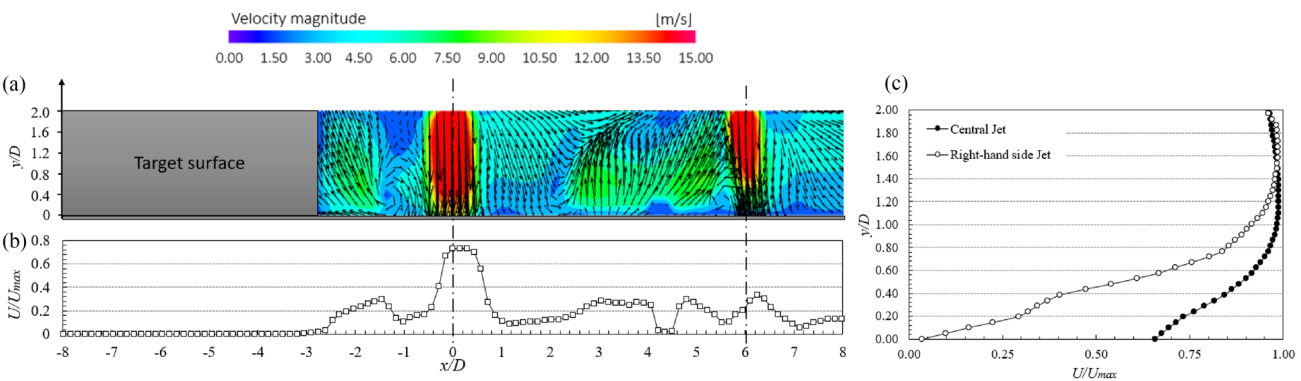
Fig. 9. 2 D step plate case velocity profile: **a** velocity field; **b** over the target plate at $y/D = 0.15$; **c** at the jet's axes

an increase in velocity at $x/D = -3$ and 3, as clearly identified in Fig. 7a. Looking at Fig. 7c, the velocity profile at the jet axis shows that higher velocities are recorded at the jet axis, supporting the previous statement.

As the complexity of the target plate increases, the measurements capture stronger flow interactions. Similar results are obtained near the target plate for 1 D and 2 D step plates, as it can be seen in Figs. 8b and 9b, with higher velocities

recorded at the central jet. However, higher velocities are identified at the central jet axis of the 2 D step plate, Fig. 9c, which is mainly due to the flow reversal induced near the step, increasing the flow turbulence in the vicinity of the central jet ($x/D = 0$). The vortex promotes the mixing which enhances the heat transfer in the central jet stagnation region, as also observed by Weigand and Spring (2011). Even if the step affects the flow development for the case of the 1 D step

plate, the step corner deflects the central jet flow, decreasing its velocity.

### 3.2.2 Time-averaged vorticity and turbulence intensity

The vorticity field is a parameter widely used to identify coherent structures and to capture the local swirling motion typical for a vortex, but also the shear (Geers et al. 2005), being previously expressed by Eq. (17). Considering that a 2D-PIV system is used in this work, a two-dimensional representation of the vorticity magnitude is presented for each plate geometry from Figs. 10, 11 and 12. The vorticity magnitude is nondimensionalized by the maximum value measured. Therefore, positive values indicate counterclockwise flow rotation while negative values imply clockwise flow rotation.

The results show that maximum values are obtained at the jet's shear layer, starting immediately downstream of the orifice edges, highlighting once again the strong flow

mixing between the jet's flow and the surrounding air. Since the nozzle-to-plate distance is small, the vorticity profile at the jet edges is kept through its full length, showing the influence of the confinement on the vortex generation. However, it is not possible to identify the variation of the vortex structures which is explained by the fact that vorticity is sensitive to both shear and local swirling motion (Geers et al. 2005). Intense stretching is captured near the stagnation point and the jet's thickness increases with the distance from the stagnation point which characterizes the wall jet region. This typical jet structure was also captured by Song and Prud'homme (2007) and (Angioletti et al. 2003). In addition, higher vorticity is observed on the left-hand side of each jet, showing the effect of the jet-induced crossflow, flowing in direction to the outlet (right-hand side). This crossflow is intensified by the step that blocks the flow on the left-hand side. The typical horseshoe vortex structure is clearly identified on the left-hand side of each jet while on the right-hand side, this structure is degraded mainly due to the flow
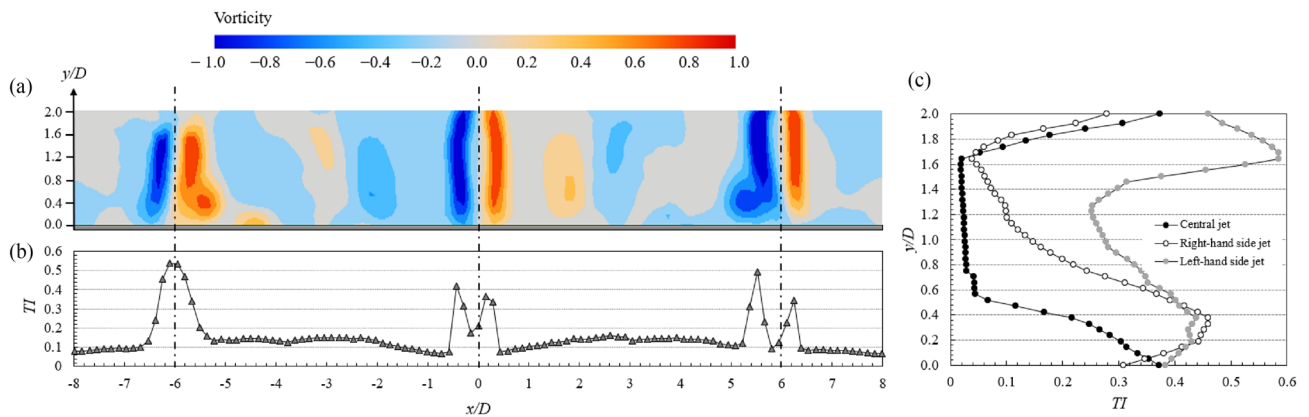
Fig. 10 Flat plate case turbulence characteristics: **a** vorticity magnitude; **b** turbulence intensity at $y/D = 0.15$; **c** turbulence intensity at the jet's axes
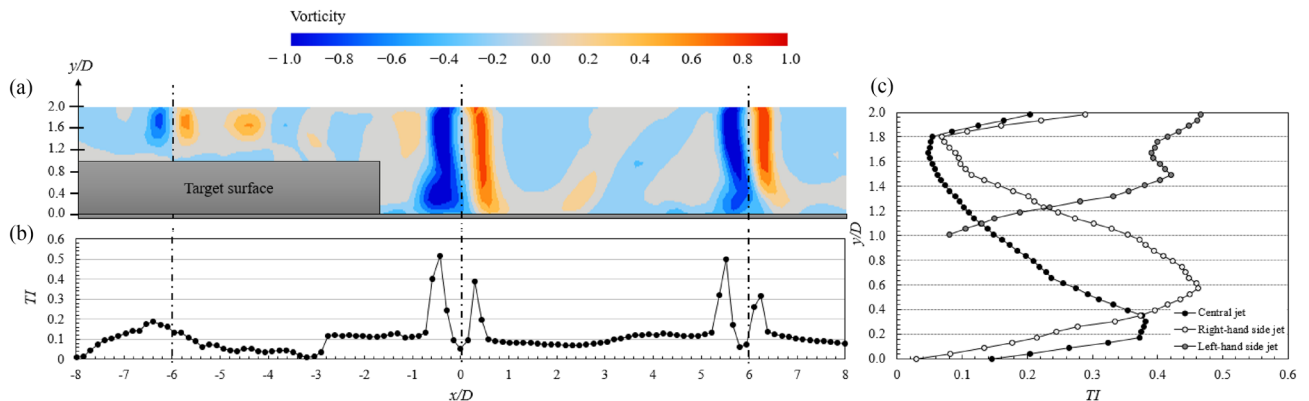
Fig. 11 $1\,D$ step plate case turbulence characteristics: **a** vorticity magnitude; **b** turbulence intensity at $y/D = 0.15$; **c** turbulence intensity at the jet's axes
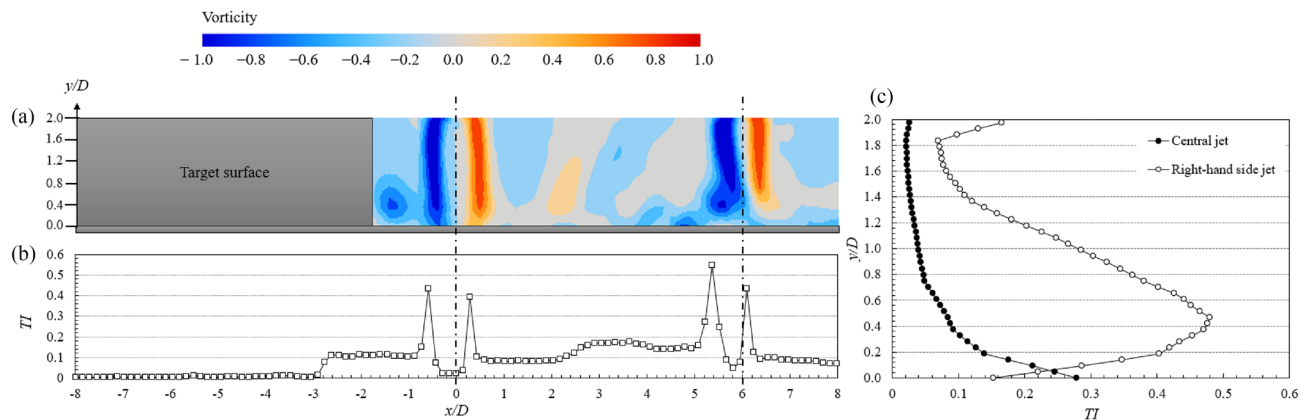
Fig. 12 2 D step plate case turbulence characteristics: **a** vorticity magnitude; **b** turbulence intensity at $y/D = 0.15$; **c** turbulence intensity at the jet's axes

deflection generated by the strong effects of the jet-induced crossflow. Moreover, high vorticity levels are reached near the step by the jet located at $x/D = 0$ at the central row, which is in agreement with the data presented by the velocity field. As previously mentioned, the 2 D step produces a flow reversal, leading to the generation of a strong vortex in the vicinity of the plate as demonstrated in Fig. 12a. Regarding the 1 D step, Fig. 11a shows a stronger horse-shoe vortex when compared with the other geometries, while in the flat plate case, two symmetric and weak vortices are induced at both sides of the central jet, as clearly identified in Fig. 10a.

To complement the analysis, the time-average turbulence intensity, nondimensionalized by the maximum velocity recorded at the jet's inlet (U_{max}), was plotted for each case in the vicinity of the target plate and at the jet's axes. This parameter is given by Eq. (18), where u_{RMS} and v_{RMS} represent the root mean square x-velocity and y-velocity, respectively.

$$\text{TI} = \left(\sqrt{u_{RMS}^2 + v_{RMS}^2} \Big/ U_{max} \right) \tag{18}$$

Focusing on the flat plate case, the data presented in Fig. 10b show that higher turbulence intensity is recorded at the adjacent jet, on the left-hand-side. This behavior is slightly different from the expected one since a similar profile to the right-hand-side jet, with higher TI, where the vortex horse-shoe is located, should be observed. Moreover, the effect of the central jet interaction on the adjacent jet's flow development is clearly identified in Fig. 10c, since higher turbulence is detected upstream of the impingement in both left and right-hand-side jets. These data are in agreement with Fig. 10b since higher turbulence intensity is measured at the left-hand-side jet. As expected, higher levels of turbulence occur at the stagnation region, at $y/D < 1$, in which the flow experiences non-uniform turning and a strong

stretching of the vortices, which increase the turbulence. However, as presented in Fig. 10c, turbulence intensity in this region is about 30% higher for the adjacent jets compared with the central jet, highlighting once again the effect of the jet-induced crossflow and wall jet's interactions on the increased intensity of the flow over the wall.

As far as the 1 D step plate is concerned, the results demonstrate that, compared with a flat plate, the left-hand-side jet flow, is highly compressed against the nozzle plate due to the reduced distance between the step and the upper plate ($y/D = 1$). Therefore, higher TI values should be expected but this is not the case, as it can be observed in Fig. 11b and c. This must be due to the reduced accuracy of the images captured by the PIV system, due to the small space between the step and the nozzle plate, which induce some optical interference near the wall. Focusing on the central jet, Fig. 11c, data show that higher turbulence intensity is recorded at the jet axis compared with the 2 D step plate, Fig. 12c. This is mainly explained by the strong deflection induced by the step corner, which does not occur in the 2 D step case. However, the behavior of the right-hand-side jet is similar in both cases. Compared with the flat geometry, the turbulence intensity at the central jet is around 25% higher for the 1 D step, while for the 2 D step, this increase reaches 7.5%. Moreover, in the vicinity of the central jet axis, turbulence intensity is more uniform and about 30% higher between $0.5 < x/D < 1.2$, compared with the flat plate. Such higher turbulence levels, for the case of a non-flat geometry, will be expressed in heat transfer enhancement compared with the flat plate.

3.2.3 Mean Q-criterion

The second invariant of the velocity gradient tensor, Q, provides additional information to detect the vortices induced throughout the impingement. According to Melling (1997),

Q is the value by which vorticity magnitude exceeds strain rate magnitude (S) and can be expressed by Eq. (19). This equation shows that $Q > 0$ indicates rotation-dominated regions, while $Q < 0$ identify strain-dominated regions.

$$Q = \frac{1}{2}\left(\|\boldsymbol{\omega}\|^2 - \|\boldsymbol{S}\|^2\right) \tag{19}$$

The results, depicted in Fig. 13, present the Q-criterion nondimensionalized by the maximum Q value measured. Through these data, it is possible to identify, with higher detail, the vortical structures, compared with the vorticity field, since Q is not affected by the local shear.

Starting with a global analysis, the data reveals that along the jet centerline, Q is around zero, as expected. The vortices grow in size as they progress into the flow, being highly influenced by the jet's flow interactions and the jet-induced crossflow. The region characterized by the stronger shear is the stagnation region since the flow decelerates and the vortices are stretched. As the flow develops over the wall, the structures break up, and regions characterized as shear-dominated and rotation-dominated appear. This can lead to non-uniform heat transfer coefficients in the vicinity of the target surface. The Q-criterion field also demonstrates that the collision between the wall jets induces fountain flows in the middle region between jets, as it can be confirmed in Fig. 13a and b at $x/D = 3$, as well as Fig. 13c at $x/D = -3$ and $x/D = 3$, where local stagnation points are clearly identified. As observed in all cases, the jet-induced crossflow has a strong influence on the development of the vortices along the surface. This crossflow, directed to the outlets, affects the jet flow field symmetry, moves the stagnation points, and disturbs other wall jets. This effect is even more pronounced over a non-flat plate, as observed in Fig. 13. Focusing on the jets located near the outlets, while in the non-flat plate, the horseshoe vortex has a stronger magnitude on the left-hand side, for the flat-plate case, this increased value is also

observed on the right-hand side of the jet located near the right outlet.

Looking in detail to the 2D step plate case, Fig. 13a, the Q-values highlight the generation of two similar eddies at both sides of the central jet located at $x/D = 0$ and a secondary vortex with the same size, close to the left-hand side vortex, induced by the flow reversal due to the step. This is a region where high heat transfer rates are expected to occur since strong turbulence is recorded. As the flow moves toward the outlet, it encounters the wall jet of the adjacent jet and a stagnation point is identified in this collision region located at $x/D = 3$. The combination of the increased turbulence due to the 2D step geometry and the jet-induced crossflow lead to a strong deflection of the adjacent jet flow. Therefore, the stagnation point is moved to the right due to the asymmetry of the two vortices induced on both sides of the adjacent jet axis.

Even though the complexity of the flow development is also identified in the 1D step plate, Fig. 13b, some differences are observed when compared with a 2D step plate. The flow deflection induced by the step corner produces strong shear due to vortex stretching. The central jet stagnation point is moved to the right and the flow of the adjacent jet is also deflected to the right. Even if a large vortex is induced at the right-hand side of the central jet, lower turbulence is observed in the vicinity of the target plate compared with the 2D step plate.

Regarding the jet flow development over the flat plate, Fig. 13c, results show a suitable symmetry of the vortices induced at the central jet, while the stagnation point is located in line with the jet axis. This difference, when compared with a non-flat plate, is mainly due to the flow deflection due to the step as well as flow reversal that does not occur in this case. As the flow moves through the outlets, wall jet collision occurs and the effect of jet-induced crossflow leads to a deflection of the adjacent jets toward the

Fig. 13 Q-criterion: **a** 2D step plate; **b** 1D step plate; **c** flat plate
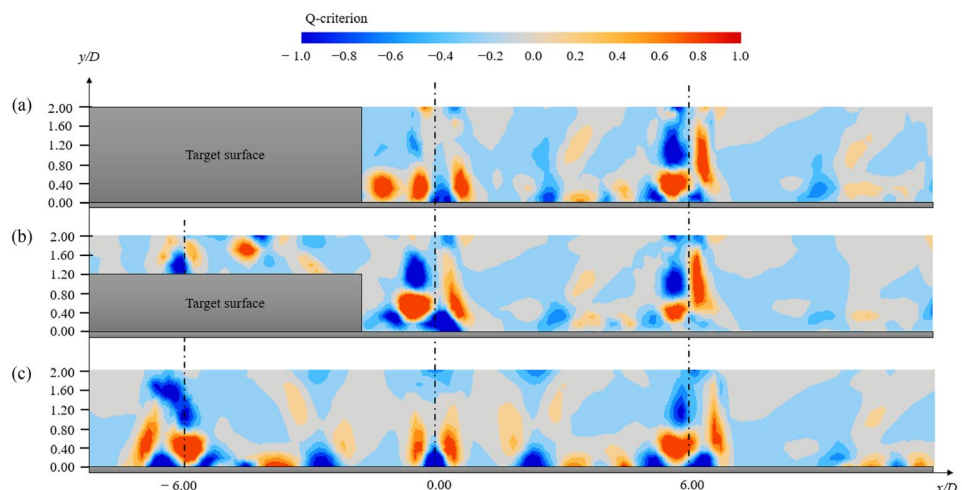
outlet. The shear regions near the wall are more pronounced in this case when compared to the non-flat plates, mainly due to a lower degradation of the flow structure.

Overall, these results show an intensification of the flow turbulence due to the step plate, therefore high heat transfer rates are expected to be obtained over a non-flat plate. This is presented in the following section.

3.3 Heat transfer

The mixing between the ambient air and the hot air that comes from the target plate is increased by the temperature difference, increasing the jet flow velocity over the surface as well as between the nozzle and the target plates. This effect promotes the heat transfer over the impinging surface and can be explained by the increase of flow driving forces in the vertical direction due to stronger buoyancy forces. While in turbulent flows the buoyancy effect can be neglected, in laminar flows the impinging regime may fall in natural, forced, or mixed convection, depending on the relative strengths of the inertia/viscous forces and the buoyancy forces involved (Nada 2009). Since the Reynolds number applied in this work is not very high, it is important to quantify the effect of natural convection on the heat transfer process. To quantify this effect, the Richardson number is determined using Eq. (20). If $Ri < < 1$ the forced convection regime is dominant, while $Ri > > 1$, natural convection prevails, and if $Ri \approx 1$, the flow is in a mixed convection regime.

$$Ri = \frac{Gr}{Re^2} \tag{20}$$

According to Nada (2009), the Grashof number (Gr) can be determined by Eq. (21):

$$Gr = \frac{g\beta * (T_w - T_\infty)H^3}{\upsilon^2} \tag{21}$$

where H is the nozzle-to-plate distance, g is the acceleration of gravity, $\beta*$ is the coefficient of volumetric expansion (for gases, $1/T$), and υ the air kinematic viscosity. In this case, the air properties are considered at film temperature.

Considering that the average temperature of the target plate (T_w) is 120 °C and the air jet temperature at the exit of the nozzle (T_∞) is 22 °C, T is equal to 71 °C, thus $\beta* = 0.014$ and $\upsilon = 1.995 \times 10^{-5}$ m²/s. These values lead to a $Gr = 33817.2$, and considering that $Re = 5000$, Ri takes a value of 0.001. These results show that, even if the Reynolds number is not very high, forced convection is dominant and the effect of natural convection is reduced.

The heat transfer performance for each plate geometry is quantified by the average Nusselt numbers obtained from the heat flux measurements, according to the scheme presented in Fig. 1f. The results are presented in Table 3, as well as the

Table 3 Average Nusselt number over the target plate

Plate configuration	$\overline{Nu}$
Flat	$29.9(0) \pm 0.45$
Non-flat—step 1 D	$32.7(2) \pm 0.49$
Non-flat—step 2 D	$37.3(9) \pm 0.56$

uncertainty of the measurement, using the analysis implemented and presented in Sect. 2.5.

The average Nusselt numbers show that the heat transfer increases as the target plate complexity increases. These observations are in agreement with the velocity, vorticity, turbulence intensity, and Q-criterion data presented in the previous sections. Near the step, where the heat flux is located, high vorticity magnitude occurs due to the strong flow reversal induced in this region. Moreover, the step increases the confinement between the nozzle and the target plates compared with the flat plate, increasing the overall turbulence intensity. This turbulence promotes the mixing between the jet's flow and the surrounding air, increasing the heat transfer rates in the vicinity of the target plate.

Although the sensor measures an average heat flux, the flow dynamics profiles allow to understand the heat transfer behavior over the area impinged by the jets and measured by the sensor. The horse-show vortex induced in the vicinity of the step entrains air, which is trapped between the jet and the step, this increases the local turbulence intensity compared to the flat plate. The vorticity profile shows that this vortex is in a clockwise rotation and increases the vorticity of the shear layer. As a result, a non-uniform heat transfer profile is expected to be induced, with higher values recorded near the step. The effect of non-uniformity of the local heat transfer is more pronounced for the case of the 1 D step plate since the deflection induced by the step corner increases the turbulence intensity on the right-hand side of the jet axis. For the case of the 2 D step plate, the increase of the local heat transfer is mainly due to the combination between a larger stagnation region and a strong flow reversal. As depicted by the Q-criterion profile, this interaction between the jet flow and the step generates two vortices, one close to the jet axis and another near the step. The collision between these two structures induces an increase in the average turbulence intensity and consequently, an increase in heat transfer. Comparing these two cases with the flat plate, a smoother flow interaction between the jets and the plate is observed. Vortices with a reduced magnitude are generated, leading to a low turbulence intensity that conducts to a lower average heat transfer in the vicinity of the wall.

The flow dynamics help to characterize the heat transfer values obtained by the heat flux sensor. Compared with the flat plate, this leads to an increase of the $\overline{Nu}$ by about 10% for the case of the 1 D step plate and by 25% for the 2 D

step plate. This difference between the 1 D and the 2 D step geometries is mainly due to the flow deflection induced by the step corner at the 1 D step plate case, which breaks up the main flow structure, reducing the heat transfer, as previously presented by the jet's flow dynamics. The increased turbulence in the vicinity of the step is more pronounced for the 2 D step case, inducing a higher average heat transfer over the target plate.

4 Conclusions

The present study describes a specially built experimental setup to conduct 2-D PIV and heat flux measurements in order to characterize the flow dynamics and heat transfer of multiple jets impinging on a surface with a step. Besides providing relevant insights regarding this complex heat transfer process, the seeding particles are also approached since they are crucial to ensure accurate PIV measurements. From the different tracking particles analyzed, olive oil proved to be the best option compared with Johnson Baby and Shell ondina oils. To characterize the jet's flow dynamics, velocity, vorticity, turbulence intensity, and the Q-criterion are the parameters used. The results highlight the flow complexity and the effect of the plate geometry on the flow development over the target plate, which is intensified by the combination between the high confinement, staggered jet pattern, and reduced distance between jets. From the analysis conducted, it was demonstrated that as the complexity of the plate geometry increases, higher turbulence intensity is recorded over the wall. The results show a horseshoe vortex with a strong magnitude at the left-hand side of the central jet due to the flow reversal induced by the step, while the central jet that impinges the flat plate presents a symmetric behavior with weaker vorticity when compared with the non-flat plates. In all cases, the effect of the jet-induced cross-flow combined with the proximity to the outlets leads to an intensification of the flow turbulence, clearly expressed by the strong magnitude of the vortices produced at both sides of the jet located near the outlet. The occurrence of these physical phenomena leads to an increase of the heat transfer by about 10% for the case of the 1 D step plate and by 25% for the 2 D step surface, compared with the flat plate.

Author's contribution Conceptualization, JT and ST; methodology, formal analysis, and investigation, FB; resources, JT and ST; writing—original draft preparation, FB; writing—review and editing, JT, ST; supervision, JT and ST; project administration, JT. All authors have read and agreed to the published version of the manuscript.

Availability of data and materials Not applicable.

Declarations

Ethical approval Not applicable.

Conflict of interest The authors declare no conflict of interest. The funders had no role in the design of the study; in the collection, analyses, or interpretation of data; in the writing of the manuscript, or in the decision to publish the results.

References

Angioletti M, Di Tommaso RM, Nino E, Ruocco G (2003) Simultaneous visualization of flow field and evaluation of local heat transfer by transitional impinging jets. Int J Heat Mass Transf 46:1703–1713

ASME (1998) Test uncertainty. Instruments and appartus. The American Society of Mechanical Engineers, New York

Assaad MC, Kimble B, Huang Y, Burgan R (2008) Thin film heat flux sensor for measuring film coefficient of rubber components of a rolling tire. Tire Sci Technol 36:275–289

Barbosa FV, Sousa SDT, Teixeira SFCF, Teixeira JCF (2021) Application of Taguchi method for the analysis of a multiple air jet impingement system with and without target plate motion. Int J Heat Mass Transf 176:121504

Barbosa FV, Teixeira SFCF, Teixeira JCF (2022) 2D PIV analysis of the flow dynamics of multiple jets impinging on a complex moving plate. Int J Heat Mass Transf 188:122600

Barbosa FV, Teixeira SFCF, Teixeira JCF (2023) Convection from multiple air jet impingement—a review. Appl Therm Eng 218:119307

Basset AB (1888) A treatise on hydrodynamics. Deighton, Bell & Co, Cambridge

Brakmann R, Chen L, Weigand B, Crawford M (2016) Experimental and numerical heat transfer investigation of an impinging jet array on a target plate roughened by cubic micro pin fins. J Turbomach 138(11):111010

Caliskan S, Baskaya S, Calisir T (2014) Experimental and numerical investigation of geometry effects on multiple impinging air jets. Int J Heat Mass Transf 75:685–703

Cengel YA, Ghajar AJ (2011) Heat and mass transfer: fundamentals and applications. McGraw-Hill Education, New York

Costa JMG (2015) Numerical simulation of the reflow soldering process. M.S. dissertation, Department of Mechanical Engineering, University of Minho, Guimarães, Portugal

Ekkad SV, Singh P (2021) A modern review on jet impingement heat transfer methods. J Heat Transf 143(6):1–15

Eshel G, Levy G, Mingelgrin U, Singer M (2004) Critical evaluation of the use of laser diffraction for particle-size distribution analysis. Soil Sci Soc Am J 68:736–743

Geers LFG, Tummers MJ, Hanjalić K (2004) Experimental investigation of impinging jet arrays. Exp Fluids 36(6):946–958

Geers LFG, Tummers MJ, Hanjalić K (2005) Particle imaging velocimetry-based identification of coherent structures in normally impinging multiple jets. Phys Fluids 17(5):1–13

Gnanamanickam EP, Bhatt S, Artham S, Zhang Z (2019) Large-scale motions in a plane wall jet. J Fluid Mech 877:239–281

Goodro M, Park J, Ligrani P, Fox M, Moon H (2007) Effects of Mach number and Reynolds number on jet array impingement heat transfer. Int J Heat Masss Transf 50:367–380

Grant I (1997) Particle image velocimetry: a review. Proc Inst Mech Eng Part C J Mech Eng Sci 211(55):55–76

Hinze JO (1975) Turbulence, McGraw-Hill classic textbook reissue. McGraw-Hill, New York

Ichikawa Y, Kameya Y, Honami S (2016) Three-dimensional flow characterization of a square array of multiple circular impinging jets using stereoscopic PIV and heat transfer relation. J vis 19(1):89–101

Khayrullina A, van Hooff T, Blocken B, van Heijst GJF (2017) PIV measurements of isothermal plane turbulent impinging jets at moderate Reynolds numbers. Exp Fluids 58(4):1–16

Kowalczuk PB, Drzymala J (2016) Physical meaning of the Sauter mean diameter of spherical particulate matter. Part Sci Technol 34(6):645–647

Le Song G, Prud'homme M (2007) Prediction of coherent vortices in an impinging jet with unsteady averaging and a simple turbulent model. Int J Heat Fluid Flow 28(5):1125–1135

Li Y, Li B, Qi F, Cheung SCP (2018) Flow and heat transfer of parallel multiple jets obliquely impinging on a flat surface. Appl Therm Eng 133(March 2018):588–603

Livingood JNB, Hrycak P (1973) Impingement heat transfer from turbulent air jets to flat plates: a literature survey, Cleveland, Ohio, USA, NASA Technical Memorandum (NASA TM X-2778), May 1973

Lo YH, Liu YH (2018) Heat transfer of impinging jet arrays onto half-smooth, half-rough target surfaces. Appl Therm Eng 128:79–91

Melling A (1997) Tracer particles and seeding for particle image velocimetry. Meas Sci Technol 8(12):1406–1416

Merzkirch W (1987) Flow visualization. Academic Press, Inc., London

Nada SA (2009) Buoyancy and cross flow effects on heat transfer of multiple impinging slot air jets cooling a flat plate at different orientations. Heat Mass Transf 45:1083–1097

Nebuchinov AS, Lozhkin YA, Bilsky AV, Markovich DM (2017) Combination of PIV and PLIF methods to study convective heat tansfer in an impinging jet. Exp Therm Fluid Sci 80:139–146

Ren Z, Yang X, Lu X, Li X, Ren J (2021) Experimental investigation of micro cooling units on impingement jet array flow pressure loss and heat. Energies 14:4757

Sahasrabudhe SN, Rodriguez-martinez V, Meara MO, Farkas BE, Sahasrabudhe SN, Rodriguez-martinez V, Meara MO (2017) Density, viscosity, and surface tension of five vegetable oils at elevated temperatures: measurement and modeling. Int J Food Prop 20(2):1965–1981

Sciacchitano A, Wieneke B, Scarano F (2013) PIV uncertainty quantification by image. Meas Sci Technol 24(4):045302

Shariatmadar H, Mousavian S, Sadoughi M, Ashjaee M (2016) Experimental and numerical study on heat transfer characteristics of various geometrical arrangement of impinging jet arrays. Int J Therm Sci 102:26–38

Singh A, Prasad BVSSS (2020) Heat transfer and flow visualization of equilaterally staggered jet arrangement on a flat surface. In: Proceedings of the ASME 2020 turbomachinery technical conference and exposition GT 2020 June 22–26, 2020, London, United Kingdom, pp GT2020-14196

Spring S, Xing Y, Weigand B (2012) An experimental and numerical study of heat transfer from arrays of impinging jets with surface ribs. J Heat Transfer 134(8):082201

Tepe A, Uysal U, Yetisken Y, Arslan K (2020) Jet impingement cooling on a rib-roughened surface using extended jet holes. Appl Therm Eng 178(115601):1–12

Terzis A (2016) On the correspondence between flow structures and convective heat transfer augmentation for multiple jet impingement. Exp Fluids 57(9):1–14

Tsai TN (2012) Thermal parameters optimization of a reflow soldering profile in printed circuit board assembly: a comparative study. Appl Soft Comput J 12(8):2601–2613

Weigand B, Spring S (2011) Multiple jet impingement—a review. Heat Transf Res 42(2):101–142

Westerweel J (1997) Fundamentals of digital particle image velocimetry. Meas Sci Technol 8:1379–1392

Whalley DC (2004) A simplified model of the reflow soldering process. J Mater Process Technol 150:134–144

Xing Y, Spring S, Weigand B (2010) Experimental and numerical investigation of heat transfer characteristics of inline and staggered arrays of impinging jets. J Heat Transfer 132(9):092201

Yong S, Zhang JZ, Xie GN (2015) Convective heat transfer for multiple rows of impinging air jets with small jet-to-jet spacing in a semi-confined channel. Int J Heat Mass Transf 86:832–842